

## Article

# Novel Hydrophobic Nanostructured Antibacterial Coatings for Metallic Surface Protection

Cristina Lavinia Nistor <sup>1</sup>, Catalin Ionut Mihaescu <sup>1</sup>, Daniela Bala <sup>2</sup>, Ioana Catalina Gifu <sup>1</sup>,  
Claudia Mihaela Ninciuleanu <sup>1</sup>, Sabina Georgiana Burlacu <sup>1,\*</sup>, Cristian Petcu <sup>1,\*</sup>, Mariana-Gratiela Vladu <sup>3</sup>,  
Adi Ghebaur <sup>4</sup>, Lenuta Stroea <sup>5</sup> and Ludmila Otilia Cinteza <sup>2</sup>

<sup>1</sup> Polymers Department, National Institute for Research and Development in Chemistry and Petrochemistry-ICECHIM, 060021 Bucharest, Romania; cristina.nistor@icechim-pd.ro (C.L.N.); catalin.mihaescu@icechim-pd.ro (C.I.M.); catalina.gifu@icechim-pd.ro (I.C.G.); claudia.ninciuleanu@icechim-pd.ro (C.M.N.)

<sup>2</sup> Physical Chemistry Department, University of Bucharest, 030018 Bucharest, Romania; dbala@gw-chimie.math.unibuc.ro (D.B.); ocinteza@gw-chimie.math.unibuc.ro (L.O.C.)

<sup>3</sup> Department of Biotechnology, National Institute for Chemical Pharmaceutical Research and Development-ICCF, 031299 Bucharest, Romania; mari29ani@yahoo.com

<sup>4</sup> Department of Bioresources and Polymer Science, Faculty of Applied Chemistry and Materials Science, University Politehnica of Bucharest, 011061 Bucharest, Romania; adi.ghebaur@upb.ro

<sup>5</sup> Polyaddition and Photochemistry Department, Petru Poni Institute of Macromolecular Chemistry, 700487 Iasi, Romania; elenah@icmpp.ro

\* Correspondence: sabina.nitu@icechim-pd.ro (S.G.B.); cpetcu@icf.ro (C.P.)

**Abstract:** A simple and cost-efficient method to modify different surfaces in order to improve their bioactivity, corrosion and wear resistance proved to be sol-gel coatings. The silane layers have been shown to be effective in the protection of steel, aluminum or magnesium alloys and copper and copper alloys. Moreover, it has been found that the adding of different inorganic nanoparticles into silica films leads to increasing their performance regarding corrosion protection. In this study, we fabricated, a simple sol-gel method, transparent mono- and bi-layered hydrophobic coatings with simultaneous antibacterial, hydrophobic and anti-corrosive properties for the protection of metallic surfaces against the action of air pollutants or from biological attacks of pathogens. The first layer (the base) of the coating contains silver (Ag) or zinc oxide (ZnO) nanoparticles with an antibacterial effect. The second layer includes zinc oxide nanoparticles with flower-like morphology to increase the hydrophobicity of the coating and to improve corrosion-resistant properties. The second layer of the coating contains a fluorinated silica derivative, 1H,1H,2H,2H-perfluorooctyl triethoxysilane (PFOTES), which contributes to the hydrophobic properties of the final coating by means of its hydrophobic groups. The mono- and bi-layered coatings with micro/nano rough structures have been applied by brushing on various substrates, including metallic surfaces (copper, brass and mild steel) and glass (microscope slides). The as-prepared coatings showed improved hydrophobic properties (water CA > 90°) when compared with the untreated substrates while maintaining the transparent aspect. The corrosion resistance tests revealed significantly lower values of the corrosion rates recorded for all the protected metallic surfaces, with the lowest values being measured for the bi-layered coatings containing ZnO particles, both in the first and in the second layers of the coating. Considering the antibacterial activity, the most effective were the AOAg-II and AOZnO-II coatings, which exhibited the highest reduction of microbial growth.

**Keywords:** hydrophobic coating; metallic surfaces protection; corrosion; wear; erosion; antimicrobial properties; in situ sol-gel



**Citation:** Nistor, C.L.; Mihaescu, C.I.; Bala, D.; Gifu, I.C.; Ninciuleanu, C.M.; Burlacu, S.G.; Petcu, C.; Vladu, M.-G.; Ghebaur, A.; Stroea, L.; et al. Novel Hydrophobic Nanostructured Antibacterial Coatings for Metallic Surface Protection. *Coatings* **2022**, *12*, 253. <https://doi.org/10.3390/coatings12020253>

Academic Editor: Judit Telegdi

Received: 21 December 2021

Accepted: 11 February 2022

Published: 15 February 2022

**Publisher's Note:** MDPI stays neutral with regard to jurisdictional claims in published maps and institutional affiliations.



**Copyright:** © 2022 by the authors. Licensee MDPI, Basel, Switzerland. This article is an open access article distributed under the terms and conditions of the Creative Commons Attribution (CC BY) license (<https://creativecommons.org/licenses/by/4.0/>).

## 1. Introduction

Due to their special importance in the field of engineering, a variety of protective coatings for metal surfaces have been developed in order to preserve or delay the degra-

dation processes. The biggest challenge that both scientists and economic beneficiaries have had to face, is the inability to halt corrosion, the growth of which can only be slowed down. It was observed that chemical attack is often accompanied by erosion and wear of the metal surface, which causes the physical degradation of the object [1]. In most cases, one of the following approaches is applied to prevent corrosion: (i) selecting metals with elements that enhance the surface with a corrosion-proof component during the corrosion process; (ii) adding aqueous inhibitors, which absorb highly on the metal surface and avoid the reaction with the oxidizing agent; (iii) spreading of protective coatings [2,3]. Choosing the most effective method of protection is often complicated and depends mainly on environmental conditions, coverage performance and financial cost. The latter includes not only the initial cost of application but also the replacement of corroded parts and, in some cases, the complete renewal of the protecting coat [2].

Sol-gel coatings can be an environmentally friendly alternative to other methods of obtaining protection materials. They can have some advantages, such as high mechanical, chemical and thermal stability, biological inertness, high transparency and photostability, controllable porosity, and controlled release of the embedded agents [4]. The silane films on metals are known to inhibit corrosion, primarily by forming a hydrophobic barrier coating, which reduces the transport of water and aggressive ions to the metal-coating interface. These coatings have also been one of the strategies to eliminate the use of chromates to make conversion coatings or as an additive to anodizing baths, due to the health problems for humans [5].

Nowadays, there has been a growing interest in the development of methods for coating the surface of metallic artifacts using materials that can prevent the formation of bacterial biofilm [6] and protect against pollutants corrosion, while maintaining the aesthetic properties of the substrates [7].

Nanoparticles have been used in various fields, ranging from the food industry, cosmetic industry and agricultural industry to devices like sensors, solar cells and batteries. They have also been used in antimicrobial research fields due to their high penetration power, even inside cells, and because they have excellent ligand-binding properties due to their high surface-area-to-volume ratio [8]. The use of nanoparticles as an antibacterial agent remains the focus of many current studies and considers metal nanoparticles like silver, gold, copper, iron and metal oxide nanoparticles, such as zinc oxide, copper oxide, titanium oxide and iron oxide [9–11].

Currently, silver nanoparticles (Ag NPs) are one of the most attractive inorganic antibacterial materials. The antimicrobial mechanism of Ag NPs is generally considered to imply multiple factors, targets and mechanisms [12]. It has been proved that Ag NPs capture the evolution and multiplication of many bacteria, such as *Bacillus cereus*, *Staphylococcus aureus*, *Citrobacter koseri*, *Salmonella typhii*, *Pseudomonas aeruginosa*, *Escherichia coli*, *Klebsiella pneumonia*, *Vibrio parahaemolyticus* and fungus such as *Candida albicans* by binding Ag/Ag<sup>+</sup> with the biomolecules existing in the microbial cells. Zomorodian et al reported that Ag NPs, which have small size and high dispersion potency, can easily adhere to cell walls of different microorganisms and can destroy and kill those cells by altering the permeability of the cell membrane and disrupting the function of the respiration system. In addition, the combination of Ag ions with the genomic substance of the cell, which contains sulfur, oxygen and nitrogen, leads to the interception of DNA replication [13]. Ag NPs are also widely used as antioxidant and antimicrobial agents, regardless of their preparation method. Antimicrobial activity of silver is successful in a manner that is harmless for animal cells, but very lethal for microorganisms (from fungi to viruses) [9]. Thus, it is considered that they are more toxic to microorganisms than to human beings [10]. Since the antimicrobial mechanism of the Ag NPs is complex, the physical and chemical properties, including the size, shape and surface charge of the NPs, can have a great influence on their antimicrobial activity [14,15].

Zinc oxide (ZnO) is also one of the main pillars of research in the field of nanotechnology, mainly due to its high applicability. ZnO NPs exhibit attractive antimicrobial

properties against bacteria (Gram-positive and Gram-negative) and fungi. It is widely used in many bactericidal formulations (such as ointments for controlling eczema) or in the cosmetic industry (in UV ray protection creams) [16]. They also show selective toxicity toward normal and cancerous cells, which is explained by reactive oxygen species (ROS) formation [17].

In recent years, extraordinary efforts have been made in the development of micro or hierarchically organized ZnO particles, resulting in a variety of new morphologies. Some of these new and interesting 2D and 3D structures include flowers, prismatic tips, closed pine cones, bullets, nanobelts, nanobridges, nanonails and nanoribbons. They were produced by various methods of synthesis, such as hydrothermal, solvothermal, chemical vapor deposition, ionothermal, sol-gel, direct precipitation, microwave-assisted synthesis, etc. [18]. For flower-like ZnO nanoparticles, the enhanced intensity of the photoluminescence band in the visible luminescence range is due to the higher surface interstitial defects that reduce the electrons or holes recombination [19]. The efficiency of photocatalytic antibacterial surfaces is usually limited by the absorption of light inside the coating material. Light absorption in photocatalytic surfaces can be enhanced by structuring it, leading to increased generation of reactive oxygen species and hence should improve the bactericidal efficacy. The antimicrobial activity of ZnO NPs was found to be light-independent in contrast to TiO<sub>2</sub> NPs, where light irradiation is required for achieving good antibacterial activity [20]. A second, more passive methodology to kill bacteria involves the use of sharp nanostructures that mechanically disrupt the bacterial membrane. Lately, the two mechanisms are being used simultaneously, leading to the formation of photoactive nanostructured surfaces with better antibacterial efficacy [21].

Silica-based materials are frequently used as highly hydrophobic or superhydrophobic coatings for corrosion protection [3,22,23]. Silica sol-gel hybrid coatings have the capacity to form a strong covalent bonding with the metal substrate through some condensation reactions [24]. When compared to conventional chemical vapor deposition (CVD) of SiO<sub>2</sub>, which typically requires well-controlled environments, with temperatures approaching 800 °C, the sol-gel process is very advantageous, especially due to its low-temperature and atmospheric pressure. Recently, functional sol-gel-based coatings with enhanced wettability, transparency and abrasion resistance, in addition to anticorrosion properties, are a developing field of research [25]. The versatility of sol-gel approaches allows tunable chemical and mechanical properties of the protective coatings and consequently facilitates use in various application areas. Moreover, the hydrolysis and condensation reactions of metal alkoxides in sol-gel processes can form strong chemical bonds with different metallic surfaces, enabling the formation of dense, uniform and defect-free protective films on metallic substrates [26]. It has also been reported that the sol-gel coatings can act as a barrier between the substrate and the corrosion environment and that both particles' addition and hydrophobicity are needed, and that their properties can act synergistically to greatly enhance the corrosion protective properties of the coating [27,28]. Another positive effect of particle addition is that the diffusion paths for corrosive species are prolonged [29].

In this work, our group developed transparent mono- and bi-layered coatings, with simultaneous antibacterial, hydrophobic and anti-corrosive effects to protect metallic surfaces against the action of pollutants or biological attacks with pathogens. The monolayer coatings (the base) consist of two different metallic nanoparticles with antibacterial properties (Ag and ZnO) embedded in a silica matrix. This layer is directly attached to the metallic substrate and assures good adhesion. For the bilayer coatings, a second layer is applied over the base film. This second layer contains an optimized amount of zinc oxide particles with flower-like morphology and is aimed at improving the hydrophobic character of the final coating, and also the barrier properties against the corrosive agents. The second layer ensures the obtaining of a surface with a higher hydrophobicity than that of the first layer of the coating because it contains ZnO particles with much larger dimensions and higher surface area than NPs used in the first layer. These large particles are able to significantly increase the surface's roughness. This layer also contains a chemical

agent that decreases surface energy (PFOTES). A rough surface with low surface energy is a mandatory requirement for obtaining an improved hydrophobic surface.

## 2. Materials and Methods

### 2.1. Materials

For the synthesis of the reference film (A0-I) the following reagents were used as received, without any additional purification: 3-(Trimethoxysilyl) propyl methacrylate (MPTS) (purity  $\geq 98\%$ , Sigma-Aldrich, Tokyo, Japan), trimethoxymethylsilane (MTMS) (purity  $\geq 98\%$ , Fluka, Darmstadt, Germany), maleic anhydride (MA) (purity  $\geq 98\%$ , Fluka, Cracow, Poland), titanium (IV) isopropoxide (TIP) (purity 97%, Aldrich, Darmstadt, Germany), 2-Hydroxy-2-methylpropiophenone (DAROCUR 1173) (purity 97%, Aldrich, Burlington, MA, USA). Ethanol (EtOH) (purity 96%) and hydrochloric acid (HCl) (0.1 N) were both purchased from SC Chimreactiv SRL, Bucharest, Romania.

For the syntheses of films loaded with metallic nanoparticles, in addition to the composition of the reference film, two different types of nanoparticles were added: Zinc oxide (ZnO) and silver (Ag). Also, 1H,1H,2H,2H-Perfluorooctyltriethoxysilane (PFOTES) (purity 97%, Alfa Aesar, Heysham, UK) was used as a chemical hydrophobisation agent in the second layer of coatings, along with tetraethylortosilicate (TEOS) (purity 98%, Acros Organics, Geel, Belgium). For the preparation of ZnO nanoparticles, we used: Zinc nitrate hexahydrate ( $\text{Zn}(\text{NO}_3)_2 \times 6\text{H}_2\text{O}$ ) (purity for analysis, Scharlab S.L., Barcelona, Spain), cetyltrimethylammonium bromide (CTABr) (purity  $\geq 98\%$ , Sigma, Ronkonkoma, NY, USA) and sodium hydroxide (NaOH) (purity  $\geq 98\%$ , SC Chemreactiv SRL, Bucharest, Romania), dissolved into bidistilled water, and produced using a laboratory ultrapure water purification system Milli-Q<sup>®</sup> Advantage A10 (Merck Millipore, Darmstadt, Germany). Silver bars used as electrodes for the synthesis of Ag NPs were commercial products (99.999% purity) with standard dimensions of 80 mm height and 2 mm diameter (SC Sonnenkreuz SRL, Brasov, Romania). Polyvinyl pyrrolidone PVP40 (Sigma-Aldrich Chemie GmbH, Darmstadt, Germany) was used as a stabilizer.

Three types of metallic substrates, brass (99.99%, Tianjin Blueprints Iron & Steel Co. LTD, Tianjin, China), copper (99.99%, Tianjin Blueprints Iron & Steel Co. LTD, Tianjin, China) and OL 37 mild steel (99%, SIDEX, Galati, Romania), were used in order to test the corrosion resistance of the mono and bilayer coatings covered on the metallic surfaces.

### 2.2. Experimental Methods

For the preparation of mono- and bilayer hydrophobic coatings doped with two different nanoparticles (Ag and ZnO), a sol-gel process has been performed. The single-layer coatings consisted of Ag or ZnO nanoparticles with antibacterial properties embedded in a silica matrix. This first layer is directly attached to the metallic substrate and assures good adhesion. For the bilayer coatings, a second layer is applied over the first antibacterial layer. This second layer is aimed to increase the hydrophobic character of the coating. Its composition includes an optimized amount of zinc oxide particles with flower-like morphology. The obtained coatings were deposited by brushing on different metallic surfaces, such as mild steel, copper and brass.

#### 2.2.1. Preparation of Spherical ZnO Particles

A hydrothermal method adapted from the literature was used for the preparation of spherical ZnO NPs: solutions of  $\text{Zn}^{2+}$  and  $\text{OH}^-$  precursors in a ratio of 1:5 were mixed under stirring. Then, an adequate volume of stabilizing and growth agent solution was added (in this case, CTABr was used) until a concentration of 1M was reached. The white precipitate obtained was left to mature for 12 h at 90 °C under reflux. The obtained NPs were separated by centrifugation at 3500 rpm for 5 min and washed repeatedly with water. Then they were dried in a hot air stream at 130 °C and re-dispersed in alcohol for their later use in the composition of the first layer of the coatings. The particles' diameters were in the

range 400–500 nm, measured by the dynamic light scattering technique, using a Zetasizer NanoZS instrument (Malvern Instruments Ltd., Worcestershire, UK).

#### 2.2.2. Preparation of Flower-like ZnO Particles

For the preparation of ZnO nanoparticles, a solution of 0.725 g  $\text{Zn}(\text{NO}_3)_2 \times 6\text{H}_2\text{O}$  with 1 g NaOH in 7.5 mL  $\text{H}_2\text{O}$  was prepared. This solution was kept for 30 minutes under magnetic stirring at a temperature of 90 °C. Meanwhile, a second solution consisting of 0.675 g CTABr in 4 mL of  $\text{H}_2\text{O}$  was prepared. The two solutions were mixed together in a Teflon autoclave and kept at 120 °C for 24 h. The resulted dispersion was washed 5 times with distilled water, by centrifugation. After each centrifugation cycle, the supernatant was removed and a fresh amount of distilled water was added. The wet precipitate was then transferred to a Petri dish and allowed to dry in air at room temperature. Before their use in the second layer composition, the flower-like ZnO particles were re-dispersed in ethanol, and only then the silica co-precursors (TEOS and PFOTES) were added.

#### 2.2.3. Preparation of Ag Nanoparticles

AgNPs were obtained using an electrochemical method with sacrificial anode [30]. The synthesis was adapted in our laboratory using a commercially available instrument, the Colloid Master 1000 model, (Colloidmaster GmbH, Isselburg, Germany), and was detailed described elsewhere [31]. Briefly, the two silver electrodes were connected to the voltage source of the instrument and placed in a 250 mL glass beaker filled with an adequate volume of dispersing media (distilled water or aqueous solution with stabilizer). In order to control the size and size distribution of nanoparticles PVP40 solution with a concentration of 1% was used as dispersion media in the electrochemical synthesis of Ag NPs. The instrument was set to work with the automatic settings to produce a 25 ppm concentration in the silver colloidal dispersion. The reaction was performed for a period of time for approximately 1 h, at room temperature, in the dark, under moderate stirring.

#### 2.2.4. Preparation of the Monolayer Coatings

According to the preliminary studies (not shown here), in order to obtain a homogeneous and transparent film, an optimal concentration of inorganic material (Ag or ZnO particles) was established. The particles concentrations were calculated as weight percent from the total amount of the first layer composition before its deposition on the supports. For the preparation of the monolayer coatings containing Ag NPs, 6 different particles concentrations (0.05; 0.10; 0.15; 0.20; 0.25 and 0.30% relative to the sol-gel mixture) were used. For the preparation of the monolayer coatings containing spherical ZnO NPs, 5 different concentrations were used (0.25, 0.5, 0.75, 1 and 1.25%). For each type of antibacterial nanoparticles, the optimum concentration was selected as the maximum concentration at which the final film remains transparent (does not significantly alter the appearance of the substrate on which it is deposited). Thus, for the AOAg-I coating, a concentration of 0.15 wt.% of Ag NPs was selected, while for the AOZnO-I coating, the selected concentration of ZnO NPs was 0.75 wt.%.

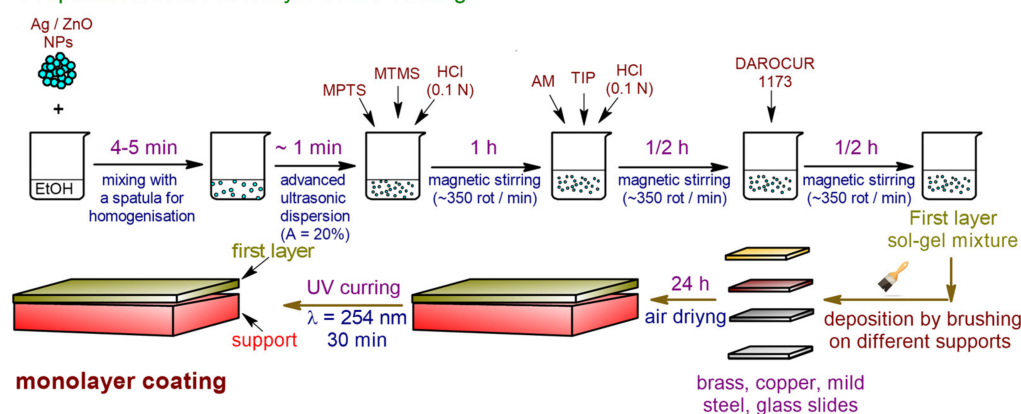
The reference monolayer film (A0-I), which does not contain inorganic particles, was prepared as follows: 2.4 g of MPTS, 2.2 g MTMS, 0.35 g HCl 0.1 N were all dissolved into 3 mL EtOH. The resulted mixture was magnetically stirred for 1 hour at room temperature. Then, 0.09 g of MA was completely dissolved into the mixture, and subsequently, 0.48 mL of TIP was drop-wisely added. Another 0.5 mL of HCl 0.1 N was also drop-wise added. This second mixture was stirred for another 30 min, followed by the addition of 0.04 g of photo initiator DAROCUR 1173. After another 30 min of stirring, the final composition was ready to be applied on various supports-glass slides and three metallic surfaces (brass, copper and mild steel).

When silver (AOAg-I coating) or zinc oxide (AOZnO-I coating) particles were added to the composition of the base film, the corresponding particles were previously dispersed in ethanol before adding the silica co-precursors and following the same procedure as

described for the A0-I reference film. For a better dispersion of the particles in ethanol, they were subjected to ultrasonication for ~1 min at an amplitude of 20%, with the aid of an ultrasonic processor, model CPX750 (Cole Parmer Instruments, Vernon Hills, IL, USA), equipped with a thin tip probe.

The metallic substrates were cut into  $0.5 \times 3 \text{ cm}^2$  pieces (metallic plates), washed with tap water and soap, and then rinsed with ethyl alcohol and dried in an oven. Each plate of brass, copper and mild steel was brushed with the final coating mixture. The coated supports were placed in an oven at  $70\text{--}80 \text{ }^\circ\text{C}$  for 3 h for fast evaporation of the solvent (EtOH), after which they were kept at room conditions for 24 h and then exposed to UV irradiation ( $\lambda = 254 \text{ nm}$ , 30 min) in order to cross-link the double bonds from methacrylate groups of MPTS (Scheme 1).

### Preparation of the first layer of the coating



**Scheme 1.** Experimental setup for preparation of the monolayer coatings (the antibacterial layer).

### 2.2.5. Preparation of Bilayer Coatings

The bi-layered coatings (A0-II, AOAg-II and AOZnO-II) were obtained by adding a second layer to the monolayer coatings described above (A0-I, AOAg-I and AOZnO-I). The second layer was prepared by dispersing 0.04 g ZnO flower-like particles, 0.6 mL PFOTES and 0.6 mL TEOS in 3 mL EtOH. This second layer was added onto the surfaces of the monolayer coatings after their exposure to UV irradiation. Before further characterization, the resulted coatings were allowed to cross-link by sol-gel process at least 24 h in the air, at room temperature (Scheme 2, Table 1).

**Table 1.** Composition of the studied coatings deposited on three different metallic supports (brass, copper, mild steel).

Monolayer Coatings		Bilayer Coatings	
Sample	Compositions	Sample	Compositions
A0-I	first layer (the base film)	A0-II	A0-I + second layer
AOAg-I	first layer loaded with Ag NPs	AOAg-II	AOAg-I + second layer
AOZnO-I	first layer loaded with ZnO NPs	AOZnO-II	AOZnO-I + second layer

### 2.3. Characterization Methods

In order to evaluate the corrosion resistance of the coatings, the protected and unprotected metallic surfaces were exposed to the corrosive action of nitrogen dioxide ( $\text{NO}_2$ ) in a sealed enclosure. The mechanically stable coatings were artificially aged for one week in an improved version of Creahan's experimental setting [32]. One of the most common polluting aerosols was chosen, nitrogen dioxide ( $\text{NO}_2$ ), with a concentration of 65.2 ppm for a relative humidity of 75%.



Commercially available scotch tape was attached to the coated films with various content of NPs, firmly pressed by hand for full contact of the solid surface, then the tape was removed. The procedure was repeated ten times before the contact angle was measured. Two other measurements were performed after 2 steps, consisting of 10 and 20 peeling cycles.

#### 2.3.4. Morphological Characterization

The morphological characterization of the coatings deposited on glass slides was performed using atomic force microscopy (AFM) and scanning electron microscopy (SEM). For the AFM analysis, the hybrid films deposited on the glass slides were scanned with an atomic force microscope Nanosurf® EasyScan 2 Advanced Research AFM type (Nanosurf, Liestal, Switzerland). The tip and cantilever used represents an integrated assembly, made of monocrystalline silicon. The properties and dimensions of the cantilever play an important role in determining the sensitivity and resolution of an AFM. The characteristics of the tip used for measurements are the following: thickness 2  $\mu\text{m}$ ; length 450  $\mu\text{m}$ ; width 50  $\mu\text{m}$ ; 13 kHz resonant frequency; pressing force 0.2 N/m. The analysis of the samples was performed in air, at room temperature (23 °C), in non-contact mode. SEM images were recorded with a Quanta 200 environmental scanning electron microscope (ESEM-FEI Quanta 200, Eindhoven, The Netherlands). The working parameters used in the study of the coating materials by SEM were the following: low vacuum, magnification between 200–12,000 $\times$ , spot value 2.5.

#### 2.3.5. Nanoindentation Test

Scratch tests and mechanical properties in terms of hardness (H) and elastic modulus (E) were determined through nanoindentation tests (Nano Indenter G200, KLA Instruments, Milpitas, CA, USA). Nine indentations with 70  $\mu\text{m}$  distance between them were performed to 2000 nm penetration depth using a Berkovich diamond tip with a radius of 20 nm. The tip approaching to surface velocity was set to 10 nm/s and the strain rate was 0.05 1/s. When reaching the maximum indentation depth, the load was kept constant for 10 s, and then it was released until 10% of the maximum load and maintained for 100 s. Then, the indenter was completely withdrawn, and the sample was positioned for the next indentation test. Representative curves for elastic modulus, hardness and load versus displacement are plotted.

For the scratch tests, a cube-corner diamond tip was used. A scratch test is comprised of three steps: (1) surface pre-scan: offers information regarding the original morphology of the surface using very small loads (30  $\mu\text{N}$ ), (2) scratch profile: in this step, the load is increased from 0 to 30 mN and the scratch is performed along the surface profile path with 30  $\mu\text{m/s}$ , and (3) post-scratch profile: uses very small loads to show the residual deformation. Additionally, a profile across the residual trace in the point where the scratch load reached 20 mN was recorded.

#### 2.3.6. Antibacterial Activity

The antibacterial activity of coatings based on nanostructured hybrid materials was performed by the ASTM E2149 method (the standard method for determining antimicrobial activity, also known as the “dynamically agitated vial method”). This type of test allows the determination of the antimicrobial activity of specimens fixed on the surface of materials, such as stone, metal, glass, paper, by placing them in direct contact with microbes in suspension, in standardized concentration (Mc Farland standard 0.5), over a determined period of 24 h. Here, for the experiments performed in order to evaluate the antimicrobial potential of the obtained silica hybrid coatings, deposited on glass slides, the used bacterial standard strain was *Bacillus cereus* ICCF 103, from the microbial collection of the National Institute for Chemical-Pharmaceutical Research-Development INCDCF-ICCF, Bucharest, Romania.

The evaluation of the protective effect of the coatings was performed by comparing the results obtained for the test samples with those obtained for the control samples. Two types of control samples were used:

- (i) *negative control controls* (M−), containing only the bacterial suspension of the *Bacillus cereus* ICCF 103 strain in a standardized concentration of  $1.5 \times 10^8$  CFU/mL (Mc Farland standard 0.5);
- (ii) *positive control controls* (M+), containing the reference nanostructured hybrid coatings (without nanoparticles) deposited on a glass slide (A0-I film), immersed in the bacterial suspension in standardized concentration (Mc Farland standard 0.5).

The media used in the experiments were as follows:

- nutrient agar (AN) medium, containing (% g/vol): peptone 0.5, yeast extract 0.15, meat extract 0.15, NaCl 0.5, agar 1.5, with pH adjusted to 7;
- the liquid medium had the same composition, except agar.

In the application of the ASTM E2149 method for the verification of the antimicrobial activity of the coatings, the AN medium and the 0.3 mM  $\text{KH}_2\text{PO}_4$  buffer were used.

During the antibacterial activity test, two successive passages on nutrient agar medium were performed. Then, the media were incubated for 24 h at 37 °C. The initial microbial suspensions of  $1.5 \times 10^8$  CFU/mL (0.5 McFarland density) were obtained from fresh cultures and were inoculated by spreading on the Petri dish agar medium. After 10 min, the plates were incubated for 16–18 h at room temperature.

Decimal dilutions were made from each collected sample and Petri dishes with AN medium were inoculated with them to calculate the colony forming units (CFU). The inoculated plates were thermostated at 30 °C for 24 h to develop the colonies. The antimicrobial effect was calculated as the difference between the initial cell concentration (calculated at the time of inoculation) and that obtained after the exposure time of the microorganism tested to the action of films containing nanoparticles. The vial containing only the microbial strain (M−), in standardized concentration, was processed in the same way as the other samples so that the possible decrease in cell concentration was related to the action of the coating materials, not to the lack of nutrients in the buffer medium.

### 3. Results

#### 3.1. Morphological Characterization

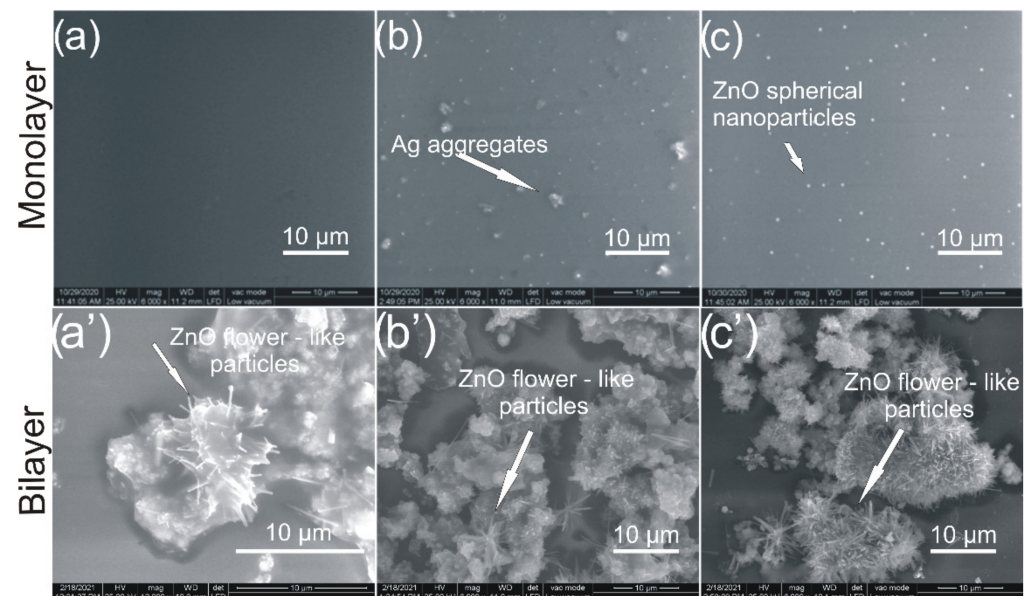
For the morphological characterization (AFM and SEM images), the mono- and bilayer coatings prepared in this study were deposited by brushing on microscope glass slides, in the form of thin films. AFM and SEM studies began with the analysis of the surface of mono-layer (A0-I) and bi-layer (A0-II) control coatings. As expected, the surface morphology of the reference film A0-I (Figures 1a and 2a) reveals a smooth aspect. The SEM (Figure 1a') and AFM (Figure 2a') images of bi-layered coating A0-II showed a well-balanced surface relief, characterized by a relatively uniform morphology and a value of the square mean roughness (Sq) of 9.63 nm. The results obtained by the SEM images revealed that the flower-like ZnO particles from the second layer of the coatings do not uniformly cover the first layer, but present discontinuities. These are due to the tendency of the particles to aggregate, following the evaporation of the solvent during the formation of the silica film. The presence of these discontinuities affects the surface roughness and, implicitly, the hydrophobic properties. An increase in the amount of particles added to the sol-gel mixture of the second layer of the coating would favor a better coating of the surface, but, at the same time, it would affect the degree of transparency of the coating. For uses that do not require the protective coating to be transparent, larger amounts of particles may be added.

For the coatings containing only the first layer, but loaded with Ag NPs or ZnO NPs (AOAg-I, Figures 1b and 2b, respectively, AOZnO-I, Figures 1c and 2c, the smooth aspect was also preserved, but the corresponding antibacterial particles can be observed, being

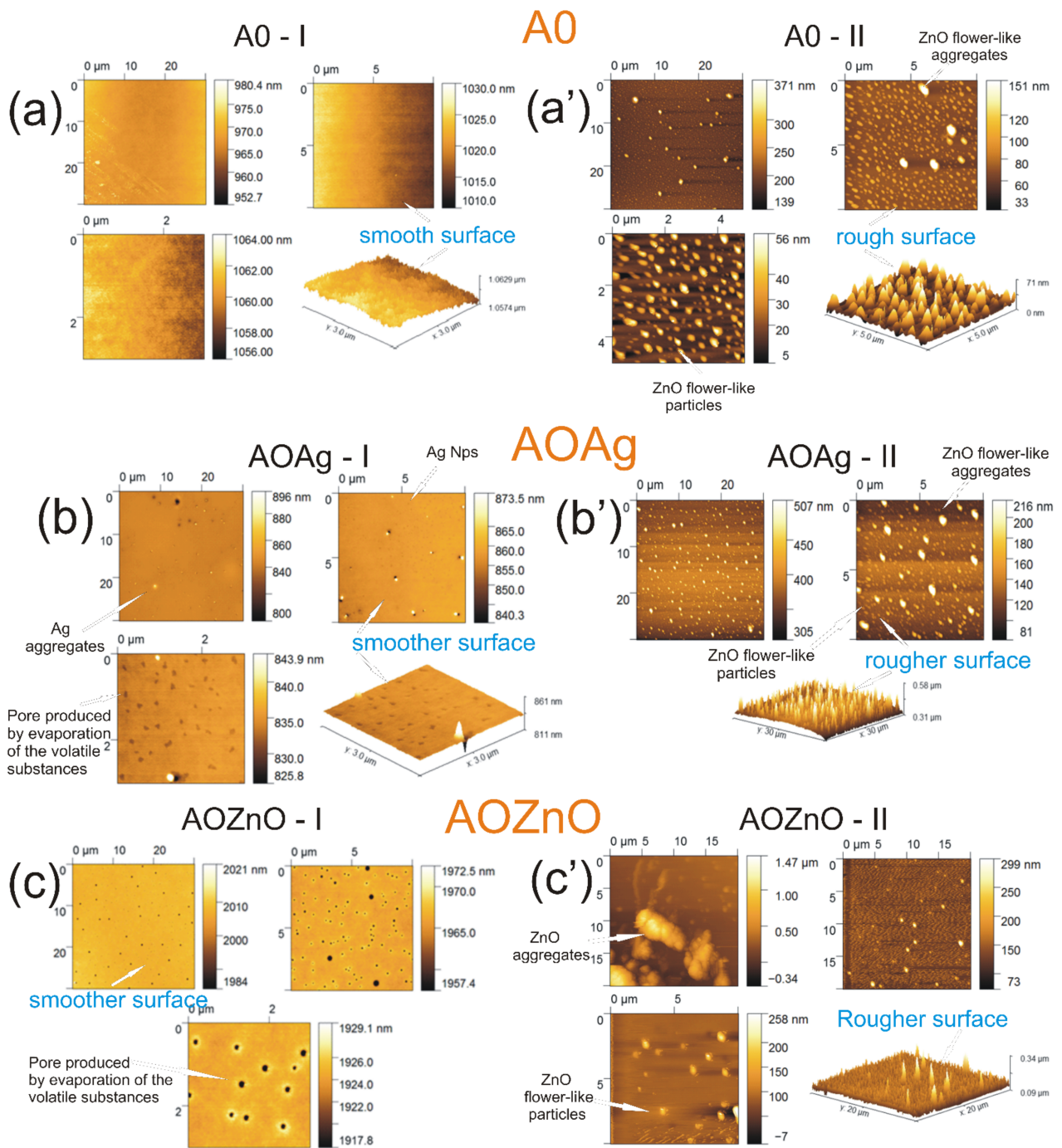
uniformly distributed inside the coating. The presence of large aggregates could also be observed for the coating AOAg-I.

Figure 1b' and Figure 2b' shows the SEM and respectively the 2D and 3D AFM images of the bilayer coating AOAg-II. It was shown quite clearly the presence of the inorganic material, silver nanoparticles being distributed densely and relatively evenly in the coating, with calculated average dimensions of ~90–120 nm and some larger particles aggregates, ~200–400 nm. Moreover, the ZnO flower-like particles and particles aggregates, with dimensions of 0.5–5  $\mu\text{m}$ , are highlighted. When compared with A0-II, the calculated average square roughness increased slightly to values of  $S_q = 16.01$  nm.

Furthermore, the morphology (Figure 1c,c') and topography (Figure 2c,c') of the mono- and bilayer coatings doped with spheric-like ZnO nanoparticles (AOZnO) were evaluated. Here, as well, the recorded 2D and 3D morphological images showed differences between the surface morphologies of the A0-II control film and the AOZnO-II doped film, due to the amount of nanostructured material found in the coating. Thus, for the AOZnO-II sample, two different areas based on the particles' different sizes were clearly highlighted. The first area contains relatively monodispersed particles, with sizes in the range of 100–150 nm, while the second area consists of aggregates with much larger diameters (>1  $\mu\text{m}$ ). These are the flower-like ZnO particles introduced into the second layer of the coating. The smooth and homogeneous morphology of the surfaces that characterize the first type of surface area was also reflected in the small values of the average square roughness ( $S_q = 17.57$  nm). A significantly increased value ( $S_q = 158.3$  nm) was recorded for the rough areas and is due to the presence of ZnO flower-like aggregates. The coating's chemical composition was evaluated by EDS analysis (Figure S1—Supplementary Information). As expected, the highest peak from the EDS spectra of the monolayer coatings is assigned to Si. Further, O and Ti are also abundant on the coating surface. However, only very weak peaks could be observed for the Ag and, respectively, ZnO particles in the EDS spectra of the AOAg-I and AOZnO-I coatings, suggesting that they are mostly embedded inside the silica film. For the bilayer coatings, the predominant signals are assigned to Zn, coming from the flower-like ZnO particles that cover the surface.



**Figure 1.** SEM images of the mono- and bilayer coatings deposited on glass slides: (a) A0-I; (a') A0-II; (b) AOAg-I; (b') AOAg-II; (c) AOZnO-I; (c') AOZnO-II.



**Figure 2.** AFM images of the mono- and bilayer coatings deposited on glass slides: (a) A0-I; (a') A0-II; (b) AOAg-I; (b') AOAg-II; (c) AOZnO-I; (c') AOZnO-II.

### 3.2. Nanoindentation and Scratching Test

When used in combination, nanoscratch and nanoindentation provide a powerful means to investigate the near-surface mechanical and tribological properties of small volumes of material. This technique enables the calculation of elastic modulus ( $E$ ) and hardness ( $H$ ) as a function of penetration depth [34]. Nanoscratch testing has the advantage that provides an experimental platform to reproduce a single point, sliding asperity contact, which is believed to control the process of abrasive wear [35]. It should be noted that the strain rate of nanoindentation tests is different from the strain rate used in traditional material tests, such as tensile tests, due to the higher stress concentration. However,

nanoindentation testing is a useful method to obtain the tendency of dependence on strain rate sensitivity [34].

Hardness (H) and elastic modulus (E) were determined through the nanoindentation test for the three monolayer coatings A0-I, AOAg-I and AOZnO-I, which, as shown by the AFM and SEM results have smoother surfaces when compared with the bi-layered coatings. For the nanoindentation test, the samples were prepared as follows: the sol-gel mixture remaining after covering the metal supports and the glass slides were poured into polyethylene trays and underwent the same treatment as the coated supports. Small shards were then taken from the resulting films (free-standing films).

Of the three samples, the highest values of H and E were recorded for the A0-I coating (H = 193 MPa and E = 2.78 GPa). Therefore, a higher load was required to reach the 2000 nm depth when compared to ZnO and Ag NPs loaded coatings (Figure 3). Despite AOZnO-I and AOAg-I recording similar values ( $H_{AOAg-I} = 64$  MPa and  $H_{AOZnO-I} = 50$  MPa;  $E_{AOAg-I} = 0.72$  GPa and  $E_{AOZnO-I} = 0.66$  GPa), AOAg-I seems to be more homogenous than AOZnO-I which, closer to the surface, recorded variations in terms of both H and E (Table 2). The load-displacement behavior is typical of that exhibited by soft material and the reduced elastic recovery indicates that the deformation occurs mainly through a plastic mechanism.

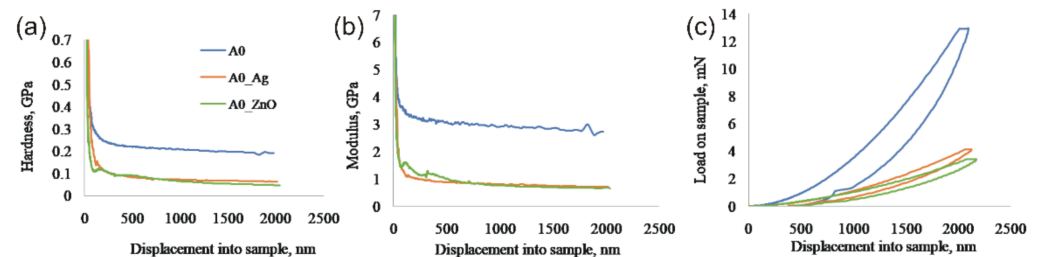


**Figure 3.** Representative curves for (a) hardness, (b) elastic modulus, and (c) load as a function of indentation depth where blue line = A0-I, orange line = AOAg-I, and green line = AOZnO-I.

**Table 2.** Values recorded for E and H at different indentation depths, results are expressed as mean  $\pm$  standard deviation, n = 9.

Sample	200 nm Indentation Depth		2000 nm Indentation Depth	
	E (GPa)	H (GPa)	E (GPa)	H (GPa)
A0-I	$3.188 \pm 0.122$	$0.265 \pm 0.047$	$2.778 \pm 0.048$	$0.193 \pm 0.004$
AOZnO-I	$1.103 \pm 0.134$	$0.097 \pm 0.024$	$0.662 \pm 0.021$	$0.050 \pm 0.002$
AOAg-I	$1.019 \pm 0.033$	$0.115 \pm 0.007$	$0.716 \pm 0.012$	$0.064 \pm 0.001$

Ramp-load scratch tests were performed on each sample to evaluate the evolution of scratch-induced damage and define the fracture evolution following the increase of normal load. The representative curves for scratch tests, the cross-section profiles obtained at 20 mN load, and the optical microscopy images of the scratch path are shown in Figure S2 (Supplementary Information). It should be mentioned that the contact depth during the experiment is defined as the difference between the initial surface topography (pre-scan) and the surface topography during scratching. Hence, the contact depth contains both elastic and plastic fractions. The scratch width contains no elastic contribution. But the scratch depth contains a significant elastic contribution and recovers during unloading [36].

The homogeneity of the A0-I film, due to the absence of Ag or ZnO particles, contributed to the avoidance of cracking along perpendicular to the scratch direction and led to a smooth penetration depth profile. As shown in Figure S2—panel III, at the entry end of the scratch groove, the groove surface maintained smooth without cracks on both sides of the groove. However, the angled facets would assist displacement of material laterally around the tip causing a pile-up effect.

For the coatings loaded with Ag or ZnO NPs, the curves became irregularly fluctuated, which mainly contributed to discontinuous brittle fracture. More than that, in the case of

AOZnO-I coating, the groove facets were more corrugated, and pile-ups, as well as flakes of debris, were responsible for the serrated profile. The penetration depth profile was clearly rougher compared with those for samples A0-I and AOAg-I. The observed cracking perpendicular to the scratch direction along the scratch groove edges was mainly attributed to the limitation of deformation ability of ZnO grains under combined effects of normal and tangential forces. These cracks tended to propagate quickly across the fractured boundaries and hence the structural integrity was disrupted. Additionally, surface damage under these pile-ups would expand to the subsurface area, as shown by Li et al. [37]. Oscillations in the penetration depth profile reflected the intermittent nature of surface damage and fracture during scratching.

Load and depth values at which fracture occurs for the three monolayer coatings are presented in Table 3.

**Table 3.** Load and depth values at which fracture occurs as well as the obtained values for pile-up which appeared after the scratch tests. Results are expressed as mean  $\pm$  standard deviation,  $n = 3$ .

Sample	Critical Load Value (mN)	Depth at Critical Load (nm)	Pile-Up Height (nm)
A0-I	2.83 $\pm$ 0.12	1579.67 $\pm$ 10.12	433.67 $\pm$ 35.53
AOZnO-I	2.86 $\pm$ 0.10	2933.00 $\pm$ 132.14	394.33 $\pm$ 79.98
AOAg-I	3.12 $\pm$ 0.25	2787.50 $\pm$ 124.39	187.75 $\pm$ 54.43

### 3.3. Peeling Tests and Contact Angles Measurements

The evaluation of the hydrophobic characteristics of the monolayer and bilayer coatings was performed by measuring the water contact angles, whose values are presented in Figure 4.

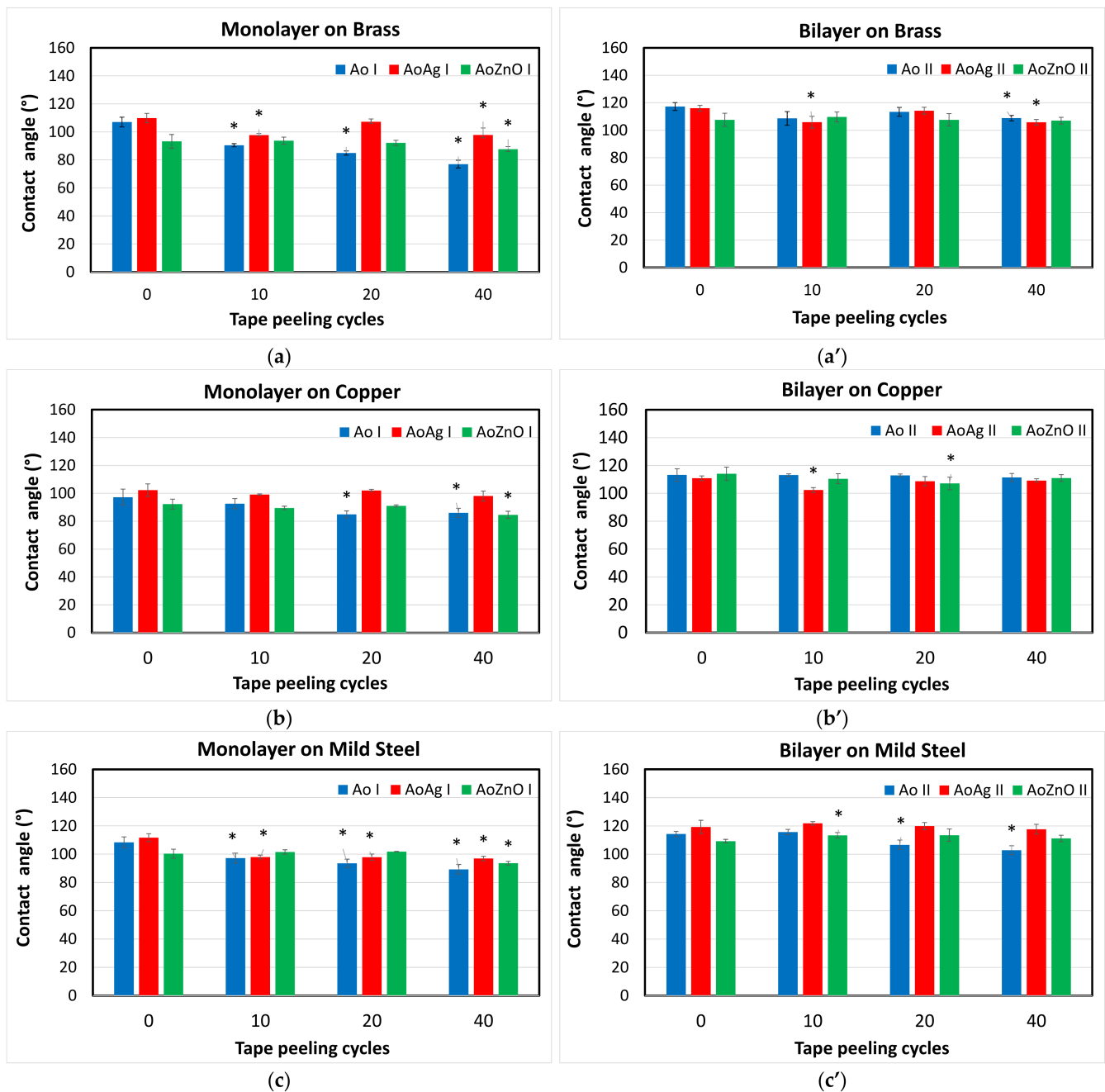
Bare/unmodified metallic coupons used as supports exhibit a low hydrophobicity, with CA ranging from 87° (Std. =  $\pm$ 2.94) for copper, 84° (Std. =  $\pm$ 3.54) for mild steel and 73° (Std. =  $\pm$ 3.10) for brass, to 90–120° after their modification (Figure S3 Supplementary Information). Deposition of mono- or bi-layered coatings results in enhancement of hydrophobicity of metallic surfaces, as is observed in Figure 4, and an increase of the values recorded for the bilayer coatings compared to the monolayer ones can be reported. It can be observed that the presence of Ag particles, which have mostly small dimensions but also form some large aggregates, can lead to a higher degree of roughness and therefore, to slightly higher values of the contact angles.

Figure 4 is showing the variation of contact angle during the tape peeling test after three steps of procedure (10 peelings, 20 and 40 peelings on the same surface of the film).

The optical images of the coatings recorded after test peeling show no evidence of visible detachment of films or particles from the samples for all metallic substrates.

The decrease in CA value is associated with the changes in adhesion and robustness of the deposited film on the metallic coupons. For the monolayer coatings deposited on brass, the CA value decreases after the first cycle of 10 peelings of tape, in the case of unmodified coating and coatings with both types of particles. Similar behavior is recorded for monolayer coatings deposited on mild steel, with the exception of monolayer containing ZnO NPs, which is more durable, with no changes in CA values after 20 cycles. All monolayer coatings, with and without NPs, exhibit the best mechanical durability when deposited on copper substrate. Unmodified coating show decreases in CA values after 20 peeling cycles, while coating with ZnO NPs exhibits changes after 20 cycles, and coating with Ag NPs exhibits no significant changes to the end of the peeling test after 40 cycles. As is expected, the adhesion of monolayer coatings depends on the metallic substrate, and it is not significantly modified by the presence of the encapsulated NPs. The adherence of the surface film to the substrate (an alloy or metal) plays a significant role, as low adherence of the surface film to the steel substrate always causes high interface energy and thus, provides instability of the interface [38]. Film formation could occur due

to the effect of the surface energy or through variations in the surface texture, as shown by Perlovich et al. [39].



**Figure 4.** The average contact angle values measured for the mono- (a–c) and bilayer (a'–c') coatings deposited on different metallic surfaces, initial and after 10, 20 and 40 peeling cycles (\*  $p < 0.05$  vs. original coated metallic substrate, before the tape peeling test).

The deposition of the second layer on the monolayer coatings to form bilayers generally increases the durability and adhesion of the coatings on all metallic substrates. The unmodified bilayer coating deposited on copper shows no significant changes during the peeling test, while deposited on brass or mild steel, the CA values decrease after 40 cycles. The bilayer coating with AgNPs (A0AgII sample) shows no changes in CA values when deposited on mild steel. In the case of the other two metallic substrates, the decrease in CA angle values after the first 10 or 20 peeling cycles, followed by the further increase, is probably due to the removal of the organic component from the surface and the increase

of the roughness, which leads to a rise of the hydrophobicity of the coating. The bilayer with ZnO NPs in the first layer (AOZnOII sample) exhibits no significant changes in CA deposited on brass, while a significant decrease is shown after 10 peeling cycles in the case of deposition on mild steel, and after 20 cycles in the case of deposition on copper. The CA values turn back in the previous range after 40 peeling cycles, due to the same detachment of superficial organic material from the coating, and the exposure of the flower-like ZnONPs, that increase the roughness. The peeling test results on the bilayer coatings suggest that the second layer deposited has good adhesion on the first one, and bilayers exhibit better durability than monolayers in terms of preservation of CA values.

### 3.4. Corrosion Resistance

Figure 5 shows the images of the metallic supports after their exposure to  $\text{NO}_2$  vapors for one week. In the left image (Figure 5a) the metallic supports are protected by our coatings, while in the right image (Figure 5b), the same type of supports were exposed uncoated. It is obvious that the prepared coatings protect all three types of metals against  $\text{NO}_2$  attack. However, when coatings doped with Ag (AOAg-II) or ZnO particles (AOZnO-II) were applied on the mild steel substrate, a slight tendency of coating's exfoliation was observed. This process is due to a weaker adhesion of the coating to this substrate.

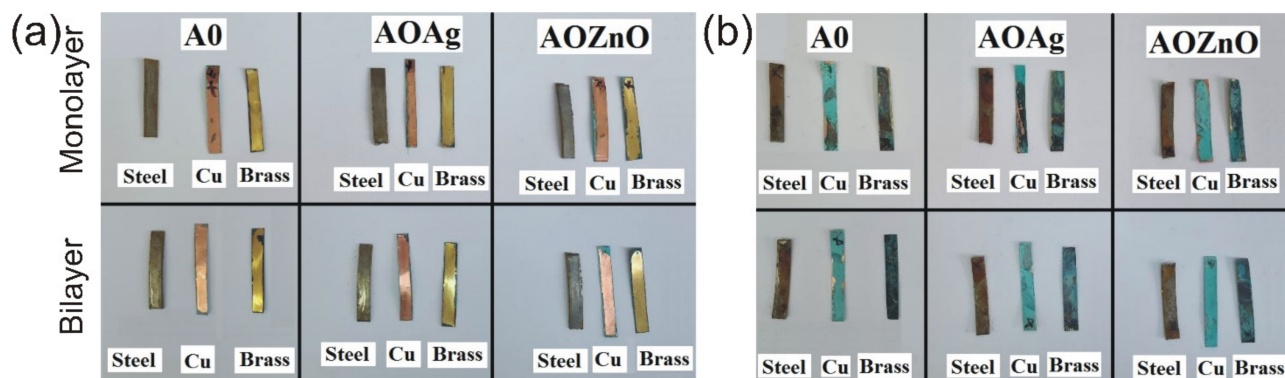


**Figure 5.** Images of brass, copper and mild steel plates after their exposure to a pollutant ( $\text{NO}_2$ ): (a) face protected with monolayer (top) and bilayer (bottom) coatings (A0 = the reference film, without nanoparticles; AOAg = film doped with Ag nanoparticles (0.15%); AOZn = film doped with ZnO nanoparticles (0.75%)) and (b) the unprotected face of the same plates.

#### 3.4.1. FT-IR Analysis

FT-IR analyses were conducted before and after exposure to  $\text{NO}_2$  to study the anti-corrosive properties of the obtained coatings. Figure S4 (Supplementary Information) shows the FT-IR spectra of the mono- and bilayer coatings, deposited on brass, copper and mild steel plates, recorded before and after  $\text{NO}_2$  exposure.

In all the FT-IR spectra of the coatings exposed to the chemical attack of  $\text{NO}_2$ , the occurrence of a new narrow and medium intensity band was noticed at  $1561\text{--}1562\text{ cm}^{-1}$ . This band can be attributed to the N–O stretching vibrations of the nitric compounds formed on the coating surface. Moreover, there is a shift and an increase in band intensity from  $1635\text{ cm}^{-1}$ , in the case of the unexposed films, to  $1645\text{ cm}^{-1}$ , after exposure to  $\text{NO}_2$ . This may be due to a contribution of the vibration  $\nu$  (ONO) of some nitrito-organic compounds. Subsequently, the band corresponding to the tensile vibration C=O exhibits a red-shift from  $1710\text{--}1720\text{ cm}^{-1}$  (where a strong influence of intra- and inter-molecular hydrogen bonds is present), towards lower energies corresponding to higher values of the wave number, up to  $1730\text{--}1735\text{ cm}^{-1}$ . One possible explanation could be that  $\text{NO}_2$  adsorbed on the surface of the coatings can inhibit the formation of hydrogen bonds, which would affect the tensile vibration of the C=O group.

Another important observation is that after comparing the spectra of films deposited on brass or copper substrates recorded before and after exposure to  $\text{NO}_2$ , very good

resistance of the coatings to chemical attack was found. However, an exception could be seen for the films deposited on mild steel plates. Thus, even though for the control film A0 the application of the second layer of the coating led to better resistance to chemical attack compared to the single-layer coating, for the bilayer coatings AOAg (II) and AOZnO (II), the presence of Ag and ZnO nanoparticles in the first layer of the coating favored a decrease of the resistance to the attack of the polluting agent. As a result, FT-IR spectra indicate a significant deterioration of the protective coatings deposited on the mild steel plates following exposure to  $\text{NO}_2$ .

### 3.4.2. Raman Analysis

For Raman analysis, coatings containing Ag nanoparticles in the first layer were deposited on brass, copper and mild steel plates. The spectra were recorded on the same samples, before and after their exposure to  $\text{NO}_2$  (Figure 6).

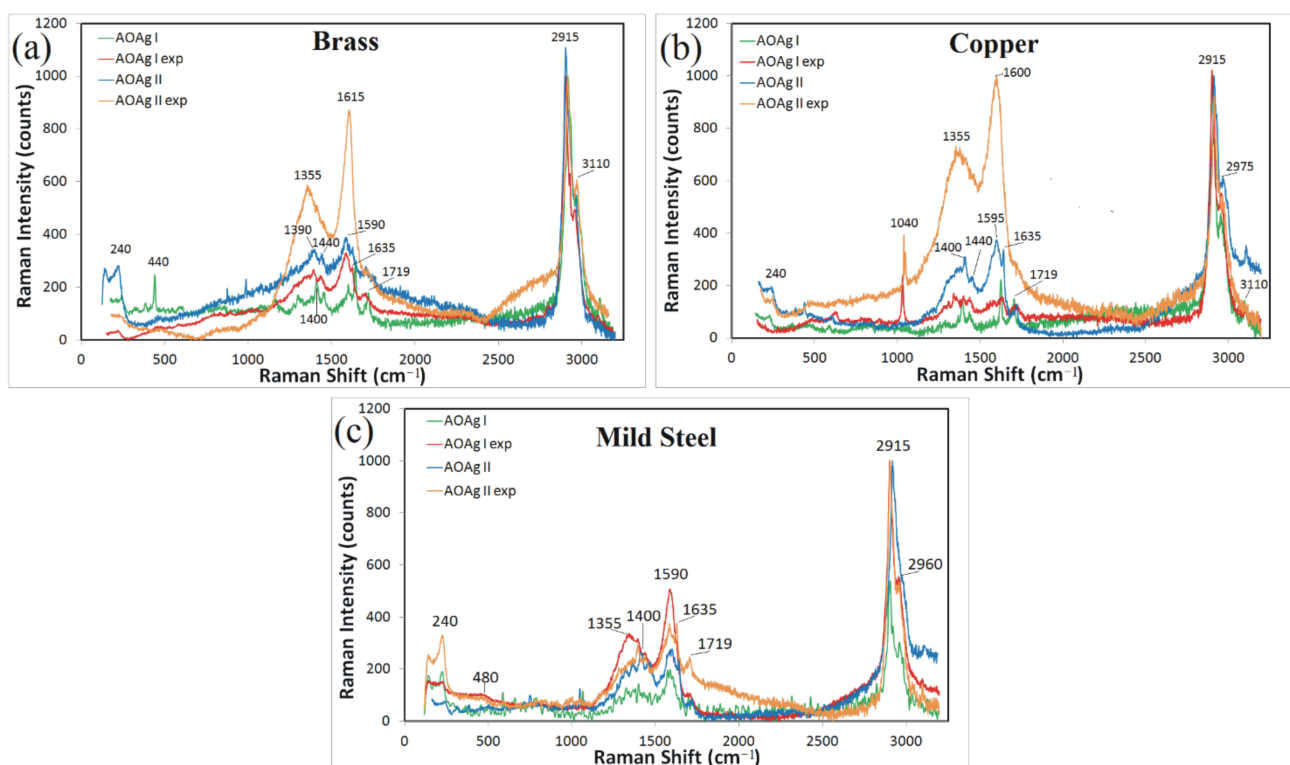


**Figure 6.** Raman spectra recorded before and after exposure to a pollutant ( $\text{NO}_2$ ) were recorded for the Ag NPs doped coatings deposited on: (a) brass plates, (b) copper plates, and (c) mild steel plates.

From the Raman spectrum recorded for the control film A0 (Figure S5—Supplementary Information) very weak signals were observed at  $\sim 440$ ,  $\sim 490$ ,  $\sim 600$  and  $\sim 800$   $\text{cm}^{-1}$ . The peak at about  $440$   $\text{cm}^{-1}$  corresponds to the R band ( $\omega_R$ ). In this low-frequency region, the band appeared due to the rocking and bending vibrations of the Si–O–Si bonds in the  $\text{SiO}_4$  siloxane tetrahedron [40]. The two weak signals from  $\sim 490$  and  $\sim 600$   $\text{cm}^{-1}$  can be attributed either to siloxane rings (consisting of silicon and oxygen atoms) with three or four members, respectively, or may be due to structural defects associated with breaking Si–O–Si bonds from the silica network (the broken bond model). Practically, the bands in this low-frequency region, between  $400$ – $700$   $\text{cm}^{-1}$ , are often associated with the Si–O–Si inter-tetrahedral connection [41]. The signal at  $\sim 800$   $\text{cm}^{-1}$  is attributed to the silica network ( $\text{SiO}_2$ ) [40]. The bands in the higher frequency region, from  $\sim 1040$  to  $1200$   $\text{cm}^{-1}$ , are due to the symmetrical stretching of silicon and oxygen in the Si–O tetrahedron, in which oxygen atoms are unbound. The signal from  $1340$   $\text{cm}^{-1}$  is attributed to the stretching vibrations

C–C from the organic components of the silica precursors, and the signal from  $1719\text{ cm}^{-1}$  comes from the stretching vibration of the carbonyl group C=O.

The wide bands at  $\sim 1400$  and  $\sim 1590\text{ cm}^{-1}$  correspond to the tensile vibrations of C=O group and C–C bond, respectively. The increase and shift in the intensity of the two Raman signals after the exposure of the coatings to the pollutant  $\text{NO}_2$  is given by the interactions that occur between the C atoms with  $\text{NO}_2$  adsorbed on the surface of the coating. Thus, the peak located at  $1350\text{ cm}^{-1}$  is attributed to the tensile vibrations of the C~N<sup>+</sup> intermediate bonds, while the intense peak from  $1600\text{ cm}^{-1}$  (for copper support) and  $1615\text{ cm}^{-1}$  (for brass support) indicates the existence of  $\delta(\text{CN})$  vibrations resulting from the formation of nitro- and nitrito- organic compounds. On the other hand, the  $1635\text{ cm}^{-1}$  band attributed to the C=C stretching vibration remains unshifted, suggesting the absence of interaction between the conjugated  $\pi$  electrons of the vinyl group from the MPTS methacryloxy- group and  $\text{NO}_2$ .

It is important to note that the presence of flower-like ZnO particles in the second layer of the coatings favors the capture of  $\text{NO}_2$  molecules on their surface. Also, the Raman spectra of the coatings deposited on mild steel plates confirm the conclusions drawn from the analysis of FT-IR spectra, that the coatings are damaged by the chemical attack of  $\text{NO}_2$  due to exfoliation.

### 3.4.3. Corrosion Inhibition

Linear sweep voltammetry (LSV) is one of the most used techniques for evaluating the corrosion phenomenon. It involves sweeping the potential applied at the working electrode and measuring the current response. With LSV, one can obtain important information concerning the corrosion rate, mechanisms of corrosion, and susceptibility of specific materials to corrosion in various types of environments. The lowest corrosion current and the highest corrosion potential values are important for the determination of corrosion resistance [42–44]. The polarization resistance ( $R_p$ ) can be used as a quantitative parameter to compare the corrosion resistance of metals under various conditions. High  $R_p$  of a metal implies high corrosion resistance and low  $R_p$  implies low corrosion resistance.

Potentiodynamic Tafel polarization curves of the bare and coated metallic surfaces (copper, brass and mild steel) were recorded after exposure to a 3.5 wt.% NaCl aqueous solution (Figure 7). The corrosion parameters including the polarization resistance ( $R_p$ ), corrosion potential ( $E_{\text{corr}}$ ), corrosion current density ( $I_{\text{corr}}$ ) and corrosion rate obtained for our treated metallic supports are given in Tables S1–S3, which are shown in the Supplementary Information section. The  $I_{\text{corr}}$  and  $E_{\text{corr}}$  values were determined using the Tafel chart. As we can see from Tables S1–S3, all coated brass, copper and mild steel substrates have higher values for  $R_p$  in comparison with the bare metals.

The modification of the corrosion rate depending on the type of coating used to protect the different metallic supports is shown in Figure 8. Almost all coated metals displayed a passivity behavior compared to bare substrates with low current densities and smaller corrosion rates. Very good properties of corrosion inhibition were exhibited by both the mono- and bi-layered A0 coatings. This insoluble and continuous film is less conductive than the metal substrate underneath, so it can reduce the rate of corrosion by retarding the charge transfer process. It also acts as a barrier between the metallic substrate and the corrosive medium. The coatings containing Ag or ZnO NPs also proved to improve the corrosion resistance properties. However, the monolayer coating AOAg-I shows a lower corrosion resistance when coated on copper or mild steel, probably due to a lower adhesion of the base layer to the substrate. Moreover, Ag NPs could be themselves subjected to a corrosion phenomenon. Moreover, the lower adhesion of the coatings to the mild steel substrate led to partial exfoliation of the coatings containing Ag or ZnO NPs and is probably the cause of the reduced corrosion passivity properties.

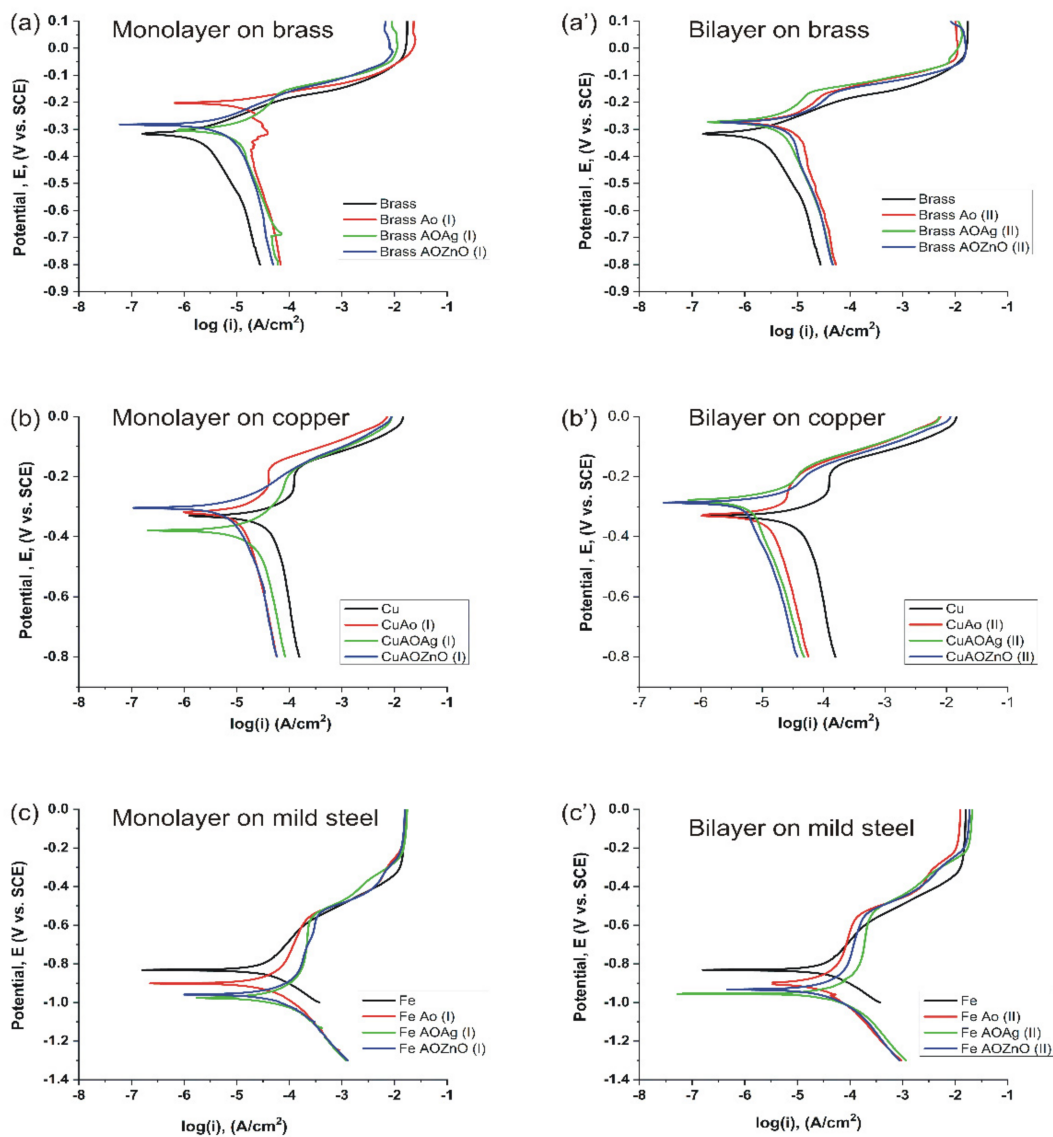


**Figure 7.** Potentiodynamic Tafel polarization curves of the bare and modified metallic surface in 3.5 wt.% NaCl aqueous solution with monolayer (a–c) and respectively, bilayer (a’–c’) coatings.

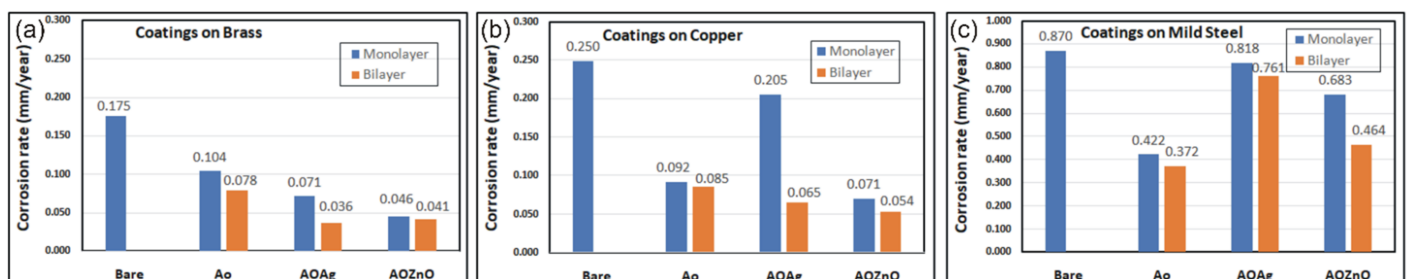


**Figure 8.** Evolution of the corrosion rate after the metallic surfaces modification: (a) brass, (b) copper, (c) mild steel.

### 3.5. Antibacterial Activity of the Coatings

The metabolic activity of microorganisms on materials such as stone, paper, metal, etc., is called biodegradation. The main way to combat this phenomenon is to cover the surfaces with films whose composition includes antimicrobial agents. In the context of the current crisis generated by the development of pathogen resistance to a wide range of antimicrobial

agents, many studies have focused on the antimicrobial activity of nanoparticles and mainly on their biocide effect. Equally important is the biostatic effect of antimicrobial agents, which induces inhibition of the development of the population of microorganisms on which they act. For verifying their efficiency, various methods of qualitative and quantitative determination of their antimicrobial effect have been developed. As a quantitative method, widely used in the evaluation of the antimicrobial activity of coatings, is the standard method ASTM E2149 [45] or various adapted or improved variants thereof.

In our study, testing the functionality of the coatings based on nanostructured hybrid materials for the protection of metal surfaces against bacteriological attacks was performed *in vitro*, by exposing the coatings deposited on glass slides to *Bacillus cereus* strain. For antibacterial tests, we used the coatings deposited on glass slides to avoid the influence of the metal supports.

Colony Forming Units Concentration at time  $t = 0$  ( $C_0$ ) was  $150 \times 10^6$  CFU/mL. After 24 h, it decreased naturally until  $43 \times 10^6$  CFU/mL ( $C_{24}$ ). In the presence of the monolayer or bilayer coatings, the CFU concentration decreases, as is shown in Figure 9. Thus, a significant reduction in cell concentration was obtained for the control sample M+ (A0-I), from  $150 \times 10^6$  to  $27 \times 10^6$  CFU/mL. This result indicates a high capacity of the reference film (not loaded with particles) to inhibit the growth of microorganisms. The addition of Ag or ZnO NPs contributed to the inhibitory effect of the monolayer coatings, but the differences are not impressive enough. This is probably due to the fact the Ag and ZnO NPs are embedded in the base film, being mostly covered by it.

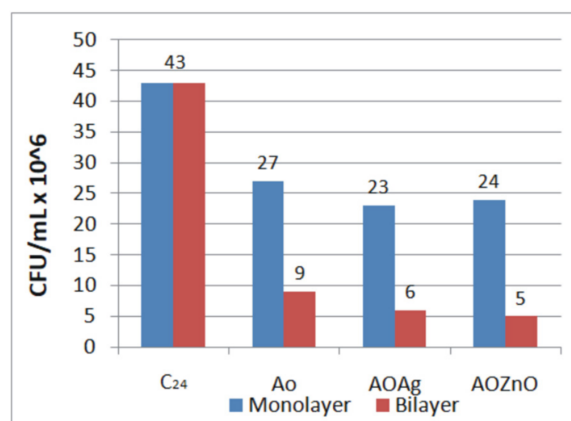


**Figure 9.** Evolution of Colony Forming Units Concentration in the presence of the mono- or bi-layered coatings.

In spite of the relatively large size of the nanocrystallites and 3D flower-like structures contained in the second layer of the coatings, all the bilayer coatings exhibited an excellent inhibitory effect on the tested strain. In particular, the most effective were the AOAg–II and AOZnO–II coatings, which exhibited the highest reduction in microbial growth. In this case, the flower-like ZnO particles are no longer embedded in the coating but are mostly situated on its surface. This allowed them to exhibit their unshielded inhibitory effect over the cell growth. A small contribution from the Ag and ZnO NPs contained in the first layer of the coatings could also be observed.

#### 4. Discussion

The mono- and bi-layered hydrophobic coatings with hierarchical micro-nano rough structures have been applied by brushing on various substrates, including metallic surfaces (copper, brass and mild steel) and glass (microscope slides). The hydrophobic surface with excellent liquid-repellent properties showed certain antibacterial functions, preventing biofilm formation. To examine the antimicrobial properties, the treated substrates were immersed in solutions containing bacteria. The adsorbed bacteria were quantified using fluorescence microscopy, showing good antimicrobial properties of both bilayer coatings

containing silver, and respectively, ZnO nanoparticles. According to the Atomic Force Microscopy (AFM) results, in the case of monolayer films observed, there was a higher surface unevenness, but a smoother aspect, and for the bi-layered films, the particles included in the coatings create a much rougher appearance. The as-prepared coatings demonstrated hydrophobic properties (water CA > 90°) of the treated metallic surfaces while maintaining the aesthetic properties of the substrates (transparent coatings). Thus, the water contact angles recorded for the bare metallic surfaces increased from 87° (Std. = ±2.94) for copper, 84° (Std. = ±3.54) for mild steel and 73° (Std. = ±3.10) for brass, to 90–120° after their modification. Moreover, the corrosion resistance tests revealed significantly lower values of the corrosion rates recorded for all the treated metallic surfaces, with the lowest values being measured for the bilayer coatings.

Wetting and spreading are familiar phenomena in nature and commonly observed in our daily life. They are of great significance for scientific research as well as for providing solutions to cutting-edge technical applications [46]. The underlying theories interpreting wetting phenomena are still mainly focused on Young's equation, the Wenzel equation and the Cassie–Baxter equation. Compared to Young's equation, the Wenzel equation extends the smooth contact surface into a rough one, and it introduces the concept of surface roughness, which makes the researchers realize the significance of the surface texture to the surface wettability [47]. Thus, Wenzel's equation proved that the hydrophobic character of a coating can be improved by creating microstructures on its surface. Based on these theories, researchers have understood that the contact angle of liquid droplets on solid surfaces is determined by both surface chemical composition and its morphology, and by combining the surface roughness with low surface energy, much improved hydrophobic properties can be obtained compared to the initial, untreated surface [47].

Corrosion and antibacterial protection of metallic parts via application of coatings have great importance in the engineering field due to applications, such as preservation of metallic heritage artifacts, protection of various metal objects exposed to pollutants in an urban environment, or protection of medical devices. In the present study, we developed new multifunctional sol-gel coatings able to protect different metallic surfaces (brass, copper or mild steel) from the corrosion of the air pollutants, such as nitrogen dioxide (NO<sub>2</sub>), and to prevent bacterial biofilm formation. An addition of some inorganic nanoparticles could enhance the antibacterial or barrier properties of the sol-gel film. The biggest challenge in designing our multifunctional coatings has been to maintain their transparency while improving their hydrophobic character. We have tried to keep the coatings transparent for those applications where it is necessary to not alter the appearance of the metal surface, as, for example, in the case of cultural heritage artifacts. It was also taken into account that the silica coatings obtained by the sol-gel process must have good adhesion to the metal support and good resistance to scratches.

In order to achieve all these goals, we designed some two-layer coatings. Thus, the first layer was designed to ensure good adhesion to the treated metal surface and to contain nanoparticles with antibacterial properties. For this purpose, we used spherical nanoparticles of Ag and ZnO. However, these nanoparticles were small in size and were internalized by silica film. As a result, they did not contribute enough to increase the roughness of the coating surface and, implicitly, to increase its hydrophobicity. Therefore, it was necessary to add a second layer, which would increase the hydrophobicity of the final coating. Hence, we chose to use flower-like ZnO particles, with much larger dimensions (~5 μm) and with a special morphology, which ensures large specific surfaces. These characteristics favor the obtaining of more rough surfaces, as shown in the SEM or AFM images presented in Figures 1 and 2. Moreover, we have considered incorporating these particles into a sol-gel film that contains a chemical agent for reducing surface energy (PFOTEOS). In fact, this second film contains only two silica co-precursors as sources for the silica film: one with perfluorinated functions (PFOTES) and one with 4 ethoxy functional groups, tetraethylorthosilicate (TEOS). The last one is necessary for a better cross-linking of the silica network and for a better reactivity to the -OH groups that are

present on the surface of the first layer of the coating. This ensures a higher hardness of the film and better adhesion to the first silica layer.

To determine the optimum particle concentration required in the sol-gel mixture corresponding to the first layer of the coating, we optimized the quantities of inorganic nanoparticles with antibacterial properties which can be added to the film so that its transparency is not visually affected. Moreso, following the nanoindentation tests (Figure 3), it was observed that with the addition of Ag or ZnO NPs in the film, its hardness decreases. Hence, although an increased amount of inorganic particles in the first layer's composition could lead to a better antibacterial activity, on the other hand, this could reduce the coating's hardness or its elastic modulus by increasing the contribution of the plastic mechanism to the strain rate. In addition, the scratching behavior of the coating is affected.

In the case of the second layer of the coating, the addition of larger amounts of flower-like ZnO particles in the sol-gel mixture could lead to more continuous coverage of the surface, but at the same time, the transparency of the final coating will be diminished.

All the prepared coatings, deposited on brass, copper or mild steel, were subjected to adhesion tests. After the 40 cycles of the tape adhesion tests, it was observed that all the bilayer coatings AOZnO-II and AOAg-II exhibited very good adhesion to the substrate, with the average values of the contact angles registering only slight decreases. The deposition of the second layer on the monolayer coatings to form bilayers generally increased the durability and adhesion of the coatings on all metallic substrates.

The coatings containing Ag or ZnO NPs also proved to exhibit similar antibacterial properties and improve the corrosion resistance properties for the treated copper or brass surfaces. However, the monolayer coating AOAg-I shows a lower corrosion resistance when coated on copper or mild steel. It was also observed that all the coatings deposited on mild steel coupons were damaged by the chemical attack of  $\text{NO}_2$ . This indicated a reduced adhesion of the coatings to this substrate, probably because of its lower surface energy. Additionally, if exposed, Ag or ZnO NPs could be themselves subjected to a corrosion phenomenon or could increase the conductivity of the corrosion current. Therefore, for certain applications, it is necessary to fine-tune the composition of the films so as to meet the requirements of use.

## 5. Conclusions

A simple, fast, cost-efficient sol-gel process was developed in order to obtain mono- and bilayer transparent coatings with antimicrobial, hydrophobic and anti-corrosive properties for metal surfaces. The results showed that silica films doped with Ag or ZnO NPs exhibit good adhesion to the metallic substrate (except mild steel) and can provide both an antimicrobial and corrosion-resistant treatment. This approach for substrate modification offers a facile and environmentally friendly means to realize biocompatible coatings for many types of substrates. The similarities between the Ag and ZnO modified coating materials indicate an excellent potential as new materials for the protection of the surface of copper or brass artifacts. In addition, the antibacterial activity of the composite film was evaluated against *Bacillus cereus* microorganisms. The results showed that the composite coatings not only have desirable hydrophobicity, good adhesion to a substrate, and favorable mechanical properties but also exhibit excellent antimicrobial activity. The multifunctional coatings developed in this study can have multiple applications, such as for the protection of cultural artifacts, for covering surfaces at risk of bacterial contamination (e.g., elevator knobs, door handles, medical devices, etc.), and for protection of various metal surfaces exposed to the attack of air pollutants, etc.

**Supplementary Materials:** The following supporting information can be downloaded at <https://www.mdpi.com/article/10.3390/coatings12020253/s1>, Table S1: LSV and corrosion parameters (from Tafel) for bare and coated copper in 3.5% NaCl, Table S2: LSV and corrosion parameters (from Tafel) for bare and coated brass in 3.5% NaCl, Table S3: LSV and corrosion parameters (from Tafel) for bare and coated mild steel in 3.5% NaCl, Figure S1: EDS spectra of the (a) monolayer and (b) bilayer coatings, Figure S2: Representative curves for panel I: scratch tests (blue line—surface pre-scan, orange line—scratch profile, yellow line—post-scratch profile); panel II: cross-section profiles obtained at 20 mN load, and panel III: optical microscopy images of the scratch path, objective 10×, Figure S3: The average contact angle values measured for the uncoated metallic coupons (bare metallic surfaces), Figure S4: FT-IR spectra recorded before and after exposure to a pollutant (NO<sub>2</sub>) for the mono- and bi-layer coatings deposited on brass, copper and mild steel plates and, Figure S5: The Raman spectrum of the reference coating A0-I.

**Author Contributions:** Conceptualization and validation, C.L.N., C.P. and S.G.B.; investigation, S.G.B., C.I.M., D.B., I.C.G., C.M.N., M.-G.V., L.S. and A.G.; writing—original draft preparation, C.L.N., L.O.C., C.I.M. and S.G.B.; writing—review and editing, L.O.C., C.P. and C.L.N.; supervision, L.O.C., C.P. and C.L.N. All authors have read and agreed to the published version of the manuscript.

**Funding:** This work was supported by a grant from the Ministry of Research, Innovation and Digitization, CNCS/CCCDI-UEFISCDI, project number PN-III-P1-1.1-TE-2019-2053, within PNCDI III, contract no. TE 85/2020 and by a grant from the Romanian National Authority for Scientific Research and Innovation, CCCDI-UEFISCDI, project number PN-III-P1-1.2-PCCDI-2017-0428 (PC2), contract no. 40PCCDI/2018-PC2, within PNCDI III.

**Institutional Review Board Statement:** Not applicable.

**Informed Consent Statement:** Not applicable.

**Data Availability Statement:** Not applicable.

**Acknowledgments:** The authors want to express their gratitude to Orha Corina from the National Institute for Research and Development in Electrochemistry and Condensed Matter-INCCEM Timisoara, for the SEM images. Additionally, the authors would like to thank Elena Olaret ([elena.olaret@upb.ro](mailto:elena.olaret@upb.ro)) for conducting the nanoindentation tests. Scratch tests and mechanical properties in terms of hardness (H) and elastic modulus (E) (Nano Indenter G200, KLA Instruments) were possible due to the European Regional Development Fund through Competitiveness Operational Program 2014–2020, Priority axis 1, Project No. P\_36\_611, MySMIS code 107066, the Innovative Technologies for Materials Quality Assurance in Health, and the Energy and Environmental Center for Innovative Manufacturing Solutions of Smart Biomaterials and Biomedical Surfaces-INOVABIOMED.

**Conflicts of Interest:** The authors declare no conflict of interest. The funders had no role in the design of the study; in the collection, analyses, or interpretation of data; in the writing of the manuscript, or in the decision to publish the results.

## References

1. Revie, R.W.; Uhlig, H.H. *Corrosion and Corrosion Control. An Introduction to Corrosion Science and Engineering*, 4th ed.; John Wiley & Sons: Hoboken, NJ, USA, 2008.
2. Figueira, R.; Fontinha, I.R.; Silva, C.J.R.; Pereira, E.V. Hybrid sol-gel coatings: Smart and green materials for corrosion mitigation. *Coatings* **2016**, *6*, 12. [[CrossRef](#)]
3. Figueira, R.B. Hybrid sol-gel coatings for corrosion mitigation: A critical review. *Polymers* **2020**, *12*, 689. [[CrossRef](#)] [[PubMed](#)]
4. Krzak, J.; Szczurek, A.; Babiarczuk, B.; Gasiorek, J.; Borak, B. Sol-gel surface functionalization regardless of form and type of substrate. In *Handbook of Nanomaterials for Manufacturing Applications*; Elsevier: Amsterdam, The Netherlands, 2020; pp. 111–147. [[CrossRef](#)]
5. García-Rodríguez, S.; Riquelme, A.; Muñoz, M.; López, A.J.; Torres, B.; Rams, J. Coating of Mg alloys and composites. In *Encyclopedia of Materials: Metals and Alloys*; Elsevier: Amsterdam, The Netherlands, 2022; pp. 75–86. [[CrossRef](#)]
6. Dulski, M.; Gawęcki, R.; Sułowicz, S.; Cichomski, M.; Kazek-Kęsik, A.; Wala, M.; Leśniak-Ziółkowska, K.; Simka, W.; Mrozek-Wilczkiewicz, A.; Gawęda, M.; et al. Key properties of a bioactive Ag-SiO<sub>2</sub>/TiO<sub>2</sub> coating on NiTi shape memory alloy as necessary at the development of a new class of biomedical materials. *Int. J. Mol. Sci.* **2021**, *22*, 507. [[CrossRef](#)] [[PubMed](#)]
7. Cao, Y.; Salvini, A.; Camaiti, M. One-step fabrication of robust and durable superamphiphobic, self-cleaning surface for outdoor and in situ application on building substrates. *J. Colloid Interface Sci.* **2021**, *591*, 239–252. [[CrossRef](#)]

8. Agarwal, H.; Nakara, A.M.; Shanmugam, V.K. Anti-inflammatory mechanism of various metal and metal oxide nanoparticles synthesized using plant extracts: A review. *Biomed. Pharmacother.* **2018**, *109*, 2561–2572. [[CrossRef](#)]
9. Agarwal, H.; Menon, S.; Kumar, S.V.; RajeshKumar, S. Mechanistic study on antibacterial action of zinc oxide nanoparticles synthesized using green route. *Chem. Interact.* **2018**, *286*, 60–70. [[CrossRef](#)]
10. Liang, T.; Wang, Y.; Zeng, L.; Liu, Y.; Qiao, L.; Zhang, S.; Zhao, R.; Li, G.; Zhang, R.; Xiang, J.; et al. Copper-doped 3D porous coating developed on Ti-6Al-4V alloys and its in vitro long-term antibacterial ability. *Appl. Surf. Sci.* **2019**, *509*, 144717. [[CrossRef](#)]
11. Fedele, D.; De Francesco, A.; Riso, S.; Collo, A. Obesity, malnutrition, and trace element deficiency in the coronavirus disease (COVID-19) pandemic: An overview. *Nutrition* **2020**, *81*, 111016. [[CrossRef](#)]
12. Li, W.; Huang, Z.; Cai, R.; Yang, W.; He, H.; Wang, Y. Rational design of Ag/ZnO hybrid nanoparticles on sericin/agarose composite film for enhanced antimicrobial applications. *Int. J. Mol. Sci.* **2020**, *22*, 105. [[CrossRef](#)]
13. Zomorodian, K.; Veisi, H.; Mousavi, S.M.; Ataabadi, M.S.; Yazdanpanah, S.; Bagheri, M.J.; Mehr, A.P.; Hemmati, S.; Veisi, H. Modified magnetic nanoparticles by PEG-400-immobilized Ag nanoparticles (Fe<sub>3</sub>O<sub>4</sub>@PEG-Ag) as a core/shell nanocomposite and evaluation of its antimicrobial activity. *Int. J. Nanomed.* **2018**, *13*, 3965–3973. [[CrossRef](#)]
14. Siddiqi, K.S.; Husen, A.; Rao, R.A.K. A review on biosynthesis of silver nanoparticles and their biocidal properties. *J. Nanobiotechnol.* **2018**, *16*, 14. [[CrossRef](#)] [[PubMed](#)]
15. Cheon, J.Y.; Kim, S.J.; Rhee, Y.H.; Kwon, O.H.; Park, W.H. Shape-dependent antimicrobial activities of silver nanoparticles. *Int. J. Nanomed.* **2019**, *14*, 2773–2780. [[CrossRef](#)] [[PubMed](#)]
16. Król-Górniak, A.; Rafińska, K.; Monedeiro, F.; Pomastowski, P.; Buszewski, B. Comparison study of cytotoxicity of bare and functionalized zinc oxide nanoparticles. *Int. J. Mol. Sci.* **2021**, *22*, 9529. [[CrossRef](#)] [[PubMed](#)]
17. Król, A.; Pomastowski, P.; Rafińska, K.; Railean-Plugaru, V.; Buszewski, B. Zinc oxide nanoparticles: Synthesis, antiseptic activity and toxicity mechanism. *Adv. Colloid Interface Sci.* **2017**, *249*, 37–52. [[CrossRef](#)] [[PubMed](#)]
18. Petcu, C.; Nistor, C.L.; Purcar, V.; Cinteza, L.O.; Spătaru, C.-I.; Ghiurea, M.; Ianchiș, R.; Anastasescu, M.; Stoica, M. Facile preparation in two steps of highly hydrophobic coatings on polypropylene surface. *Appl. Surf. Sci.* **2015**, *347*, 359–367. [[CrossRef](#)]
19. Tănase, M.; Marinescu, M.; Oancea, P.; Răducan, A.; Mihaescu, C.; Alexandrescu, E.; Nistor, C.; Jinga, L.-I.; Dițu, L.; Petcu, C.; et al. Antibacterial and photocatalytic properties of ZnO nanoparticles obtained from chemical versus *Saponaria officinalis* extract-mediated synthesis. *Molecules* **2021**, *26*, 2072. [[CrossRef](#)] [[PubMed](#)]
20. Belay, A.; Mekuria, M.; Adam, G. Incorporation of zinc oxide nanoparticles in cotton textiles for ultraviolet light protection and antibacterial activities. *Nanomater. Nanotechnol.* **2020**, *10*, 184798042097005. [[CrossRef](#)]
21. Singh, J.; Jadhav, S.; Avasthi, S.; Sen, P. Designing photocatalytic nanostructured antibacterial surfaces: Why is black silica better than black silicon? *ACS Appl. Mater. Interfaces* **2020**, *12*, 20202–20213. [[CrossRef](#)]
22. Montemor, F. Functional and smart coatings for corrosion protection: A review of recent advances. *Surf. Coatings Technol.* **2014**, *258*, 17–37. [[CrossRef](#)]
23. Artesani, A.; Di Turo, F.; Zucchelli, M.; Traviglia, A. Recent advances in protective coatings for cultural heritage—An overview. *Coatings* **2020**, *10*, 217. [[CrossRef](#)]
24. Zorinyan, M.Y.; Nashaat, A.; El-Shaer, Y.; Naeem, I.; Elzahed, O.; Gobara, M. Optimized silica-based hybrid coatings for the protection of aluminum against chloride-rich environment. *J. Sol-Gel Sci. Technol.* **2020**, *94*, 257–269. [[CrossRef](#)]
25. Khodakarami, S.; Zhao, H.; Rabbi, K.F.; Miljkovic, N. Scalable corrosion-resistant coatings for thermal applications. *ACS Appl. Mater. Interfaces* **2021**, *13*, 4519–4534. [[CrossRef](#)] [[PubMed](#)]
26. Li, Y.; Wu, C.; Xue, M.; Cai, J.; Huang, Y.; Yang, H. Preparation of sol-gel derived anticorrosive coating on Q235 carbon steel substrate with long-term corrosion prevention durability. *Materials* **2019**, *12*, 1960. [[CrossRef](#)] [[PubMed](#)]
27. Corrosion Coating—An Overview. ScienceDirect Topics. Available online: <https://www.sciencedirect-com.am.e-nformation.ro/topics/materials-science/corrosion-coating> (accessed on 15 November 2021).
28. Trentin, A.; Gasparini, A.D.L.; Faria, F.A.; Harb, S.V.; dos Santos, F.C.; Pulcinelli, S.H.; Santilli, C.V.; Hammer, P. Barrier properties of high performance PMMA-silica anticorrosion coatings. *Prog. Org. Coatings* **2019**, *138*, 105398. [[CrossRef](#)]
29. Makhlof AS, H.; Abu-Thabit, N.Y. *Advances in Smart Coatings and Thin Films For Future Industrial and Biomedical Engineering Applications*; Elsevier: Amsterdam, The Netherlands, 2019.
30. Reetz, M.T.; Helbig, W. Size-selective synthesis of nanostructured transition metal clusters. *J. Am. Chem. Soc.* **1994**, *116*, 7401–7402. [[CrossRef](#)]
31. Cinteza, L.O.; Scamoroscenco, C.; Voicu, S.N.; Nistor, C.L.; Nitu, S.G.; Trica, B.; Jecu, M.-L.; Petcu, C. Chitosan-stabilized ag nanoparticles with superior biocompatibility and their synergistic antibacterial effect in mixtures with essential oils. *Nanomaterials* **2018**, *8*, 826. [[CrossRef](#)]
32. Creahan, J. Controlling relative humidity with saturated calcium nitrate solutions. *WAAC Newsl.* **1991**, *13*, 17–18.
33. Gong, X.; He, S. Highly durable superhydrophobic polydimethylsiloxane/silica nanocomposite surfaces with good self-cleaning ability. *ACS Omega* **2020**, *5*, 4100–4108. [[CrossRef](#)]
34. Tanaka, Y.; Hattori, K.; Harada, Y. Evaluating local strain rate sensitivity of titanium alloy using dynamic nanoindentation testing. *Meas. Sens.* **2021**, *18*, 100094. [[CrossRef](#)]
35. Kareer, A.; Tarleton, E.; Hardie, C.; Hainsworth, S.V.; Wilkinson, A.J. Scratching the surface: Elastic rotations beneath nanoscratch and nanoindentation tests. *Acta Mater.* **2020**, *200*, 116–126. [[CrossRef](#)]

36. Tsybenko, H.; Farzam, F.; Dehm, G.; Brinckmann, S. Scratch hardness at a small scale: Experimental methods and correlation to nanoindentation hardness. *Tribol. Int.* **2021**, *163*, 107168. [[CrossRef](#)]
37. Li, W.; Liu, W.; Qi, F.; Chen, Y.; Xing, Z. Determination of micro-mechanical properties of additive manufactured alumina ceramics by nanoindentation and scratching. *Ceram. Int.* **2019**, *45*, 10612–10618. [[CrossRef](#)]
38. Dwivedi, D.; Lepková, K.; Becker, T. Carbon steel corrosion: A review of key surface properties and characterization methods. *RSC Adv.* **2017**, *7*, 4580–4610. [[CrossRef](#)]
39. Perlovich, Y.A.; Isaenkova, M.G.; Medvedev, P.N.; Fesenko, V.A.; Thu, S.S. Mechanisms of the texture influence on the corrosion behavior of Zr-alloy cladding tubes. *Inorg. Mater. Appl. Res.* **2015**, *6*, 259–266. [[CrossRef](#)]
40. Österle, W.; Giovannozzi, A.; Gradt, T.; Häusler, I.; Rossi, A.M.; Wetzels, B.; Zhang, G.; Dmitriev, A. Exploring the potential of Raman spectroscopy for the identification of silicone oil residue and wear scar characterization for the assessment of tribofilm functionality. *Tribol. Int.* **2015**, *90*, 481–490. [[CrossRef](#)]
41. Biswas, R.K.; Khan, P.; Mukherjee, S.; Mukhopadhyay, A.K.; Ghosh, J.; Muraleedharan, K. Study of short range structure of amorphous Silica from PDF using Ag radiation in laboratory XRD system, RAMAN and NEXAFS. *J. Non-Cryst. Solids* **2018**, *488*, 1–9. [[CrossRef](#)]
42. Demirci, E.E.; Arslan, E.; Ezirmik, K.V.; Baran, Ö.; Totik, Y.; Efeoglu, I. Investigation of wear, corrosion and tribocorrosion properties of AZ91 Mg alloy coated by micro arc oxidation process in the different electrolyte solutions. *Thin Solid Film.* **2013**, *528*, 116–122. [[CrossRef](#)]
43. Shi, X.; Wang, Y.; Li, H.; Zhang, S.; Zhao, R.; Li, G.; Zhang, R.; Sheng, Y.; Cao, S.; Zhao, Y.; et al. Corrosion resistance and biocompatibility of calcium-containing coatings developed in near-neutral solutions containing phytic acid and phosphoric acid on AZ31B alloy. *J. Alloys Compd.* **2020**, *823*, 153721. [[CrossRef](#)]
44. Chen, J.; Xu, J.; Huang, J.; Dai, L.; Xue, M.; Luo, J. Corrosion resistance of T-ZnOw/PDMS-MAO composite coating on the sintered NdFeB magnet. *J. Magn. Magn. Mater.* **2021**, *534*, 168049. [[CrossRef](#)]
45. Damian, L.; Patachia, S. Method for testing the antimicrobial character of the materials and their fitting to the scope. *Bull. Transilv. Univ. Brasov Eng. Sci. Ser. I* **2014**, *7*, 37. Available online: <http://rs.unitbv.ro/BU2013/2014/BULETIN%20I/Damian%20N.pdf> (accessed on 20 December 2021).
46. Si, Y.; Yu, C.; Dong, Z.; Jiang, L. Wetting and spreading: Fundamental theories to cutting-edge applications. *Curr. Opin. Colloid Interface Sci.* **2018**, *36*, 10–19. [[CrossRef](#)]
47. Wang, B.; Zhang, Y.; Shi, L.; Li, J.; Guo, Z. Advances in the theory of superhydrophobic surfaces. *J. Mater. Chem.* **2012**, *22*, 20112–20127. [[CrossRef](#)]